Aalborg Universitet

AALBORG UNIVERSITY

Battery impedance spectrum prediction from partial charging voltage curve by machine learning

Guo, Jia; Che, Yunhong; Pedersen, Kjeld; Stroe, Daniel Ioan

Published in:
Journal of Energy Chemistry

DOI (link to publication from Publisher):
10.1016/j.jechem.2023.01.004

Creative Commons License
CC BY 4.0

Publication date:
2023

Document Version
Publisher's PDF, also known as Version of record

Link to publication from Aalborg University

Citation for published version (APA):
Guo, J., Che, Y., Pedersen, K., & Stroe, D. I. (2023). Battery impedance spectrum prediction from partial charging voltage curve by machine learning. *Journal of Energy Chemistry*, *79*, 211-221. https://doi.org/10.1016/j.jechem.2023.01.004

General rights
Copyright and moral rights for the publications made accessible in the public portal are retained by the authors and/or other copyright owners and it is a condition of accessing publications that users recognise and abide by the legal requirements associated with these rights.

- Users may download and print one copy of any publication from the public portal for the purpose of private study or research.
- You may not further distribute the material or use it for any profit-making activity or commercial gain
- You may freely distribute the URL identifying the publication in the public portal -

Take down policy
If you believe that this document breaches copyright please contact us at vbn@aub.aau.dk providing details, and we will remove access to the work immediately and investigate your claim.

Downloaded from vbn.aau.dk on: December 06, 2025

Journal of Energy Chemistry 79 (2023) 211–221

Contents lists available at ScienceDirect

Journal of Energy Chemistry

journal homepage: www.elsevier.com/locate/jechem

http://www.journals.elsevier.com/journal-of-energy-chemistry/

Battery impedance spectrum prediction from partial charging voltage curve by machine learning

Jia Guo [a], Yunhong Che [a,*], Kjeld Pedersen [b], Daniel-Ioan Stroe [a]

[a] AAU Energy, Aalborg University, Aalborg 9220, Denmark
[b] Department of Materials and Production, Aalborg University, Aalborg 9220, Denmark

ARTICLE INFO

Article history:
Received 6 November 2022
Revised 19 December 2022
Accepted 3 January 2023
Available online 20 January 2023

Keywords:
Impedance spectrum prediction
Lithium-ion battery
Machine learning
EIS
Graphite anode

ABSTRACT

Electrochemical impedance spectroscopy (EIS) is an effective technique for Lithium-ion battery state of health diagnosis, and the impedance spectrum prediction by battery charging curve is expected to enable battery impedance testing during vehicle operation. However, the mechanistic relationship between charging curves and impedance spectrum remains unclear, which hinders the development as well as optimization of EIS-based prediction techniques. In this paper, we predicted the impedance spectrum by the battery charging voltage curve and optimized the input based on electrochemical mechanistic analysis and machine learning. The internal electrochemical relationships between the charging curve, incremental capacity curve, and the impedance spectrum are explored, which improves the physical interpretability for this prediction and helps define the proper partial voltage range for the input for machine learning models. Different machine learning algorithms have been adopted for the verification of the proposed framework based on the sequence-to-sequence predictions. In addition, the predictions with different partial voltage ranges, at different state of charge, and with different training data ratio are evaluated to prove the proposed method have high generalization and robustness. The experimental results show that the proper partial voltage range has high accuracy and converges to the findings of the electrochemical analysis. The predicted errors for impedance spectrum are less than 1.9 mΩ with the proper partial voltage range selected by the corelative analysis of the electrochemical reactions inside the batteries. Even with the voltage range reduced to 3.65–3.75 V, the predictions are still reliable with most RMSEs less than 4 mΩ.

© 2023 Science Press and Dalian Institute of Chemical Physics, Chinese Academy of Sciences. Published by ELSEVIER B.V. and Science Press. This is an open access article under the CC BY license (http://creativecommons.org/licenses/by/4.0/).

1. Introduction

Lithium-ion batteries (LIBs) are widely used in electric vehicles and portable electronic devices, due to their high energy density, long service life, and environmental friendliness [1–4]. However, the inevitable degradation of Li-ions batteries poses a big challenge to the safety during storage and usage, which urges the development and application of battery prognostic technologies [5,6]. Among them, electrochemical impedance spectroscopy (EIS) is a method for determining the impedance spectrum that can be used to present the battery health state, battery internal impedance, and the dynamic diffusion of lithium-ions (Li-ions), etc. [7,8].

EIS has been widely used to identify the parameters of the equivalent circuit model (ECM) to support the online estimation of battery states such as battery internal impedance, dynamics behavior of Li-ions diffusion, contact impedance of electrodes, state of charge (SOC) and state of health (SOH) [9,10]. The parameters of the ECM model have been proven to have a high correlation with the battery aging status. Therefore, machine learning has been used to develop algorithms to estimate the SOH and predict the lifetime of batteries by either inputting the whole EIS curve or by extracting features from the EIS curve [11,12]. Besides, the EIS result can give more physical aging meaning inside the battery, such as the diffusion of Li-ions, formation of the interface impedance, and ohmic impedance. However, the implementation of onboard EIS measurement is hindered, due to the high cost of the measurement equipment, test results subject to SOC and temperature variations, and time-demanding measurements. These limitations hinder the development of the EIS based method for online battery health prognostics. Therefore, the prediction of EIS is of vital importance to provide the impedance information for battery health prognostics. Accurate prediction via measurable parameters helps promote the advanced prognostic methods based on EIS and reduce the cost significantly. Duan et al. [13] achieved an accurate impedance spectrum prediction based on machine

* Corresponding author.
E-mail address: ych@energy.aau.dk (Y. Che).

https://doi.org/10.1016/j.jechem.2023.01.004
2095-4956/© 2023 Science Press and Dalian Institute of Chemical Physics, Chinese Academy of Sciences. Published by ELSEVIER B.V. and Science Press.
This is an open access article under the CC BY license (http://creativecommons.org/licenses/by/4.0/).

learning using complete battery charging data with a root mean squared error (RMSE) less than 1.862 mΩ. This promising prediction method can accurately estimate impedance spectrum and offer the possibility for real-time EIS based battery states estimation and health prognostics. However, there is a very limited understanding of the relationship between battery charging/discharging curves and impedance spectrum in terms of electrochemical mechanisms, which means the physical interpretability remains unclear. In addition, the partial voltage curve obtained during charging is supposed to be used considering the practical applications; furthermore, the selection of the voltage range during charging should be based on an analysis of the relationship between the voltage, incremental capacity (IC), differential voltage (DV), and EIS curves. Finally, the prediction under different SOC points is supposed to be provided for different application requirements, such as considering the impedance in battery package making.

Charging curves and EIS curves are widely used for battery health diagnosis and degradation quantification. Typically, aging mechanisms involve three degradation modes: conductivity loss (CL), loss of lithium inventory (LLI), and loss of active material (LAM) [14,15]. Compared with LLI and LAM, the CL always changes less in battery aging [16]. In practice, the charging profiles of the EVs are easily accessible, due to the controllable charging process. The charging curves can be converted to incremental capacity (IC) and differential voltage (DV) curves by the differential method. The peaks in the IC and valleys in DV curves represent specific electrochemical reaction processes occurring in both the positive electrode and negative electrode, which are usually used to quantify the LAM and LLI for the aged battery [17]. Besides, EIS also can be used for the quantification of LAM and LLI [15]. Since both charging curves and EIS can be used for quantification of LAM and LLI, a mechanism connection can be established. Then, machine learning methods can be used for estimating the impedance spectrum of the battery by charging curves.

The framework reported in this study is based on electrochemical mechanism analysis and summary to determine the existence of a correlation between charging curves and impedance spectrum, followed by a machine learning-based approach to predict the whole impedance spectrum. Specifically: (1) coin cells were assembled to clarify the electrochemical mechanisms of the IC and DV curves, which were used for quantification of LAM and LLI, and the mechanisms responsible for LAM and LLI quantification by EIS results were also analyzed; then, a quantifiable relationship between charging curves and impedance spectrum was obtained; (2) based on the mechanism analysis, the charging curve is used to achieve an accurate prediction for the impedance spectrum, and the SOC interval of the charging curve, which was used as input, was optimized; (3) impedance spectrum prediction for the battery at different SOCs were achieved; (4) the method was verified using different-testing ratios, and different machine learning methods were attempted.

2. Experimental

2.1. Dataset collection

Seven 18,650 cylindrical cells (HDCNR18650-2200–3.7 V) were aged at different temperatures and depths of discharge to achieve different aging states. The specific aging protocols and equipment were reported in our previous work[18]. After every-one hundred equivalent full cycles (EFCs), the aging of the battery is stopped and the battery is transferred to a 25 °C constant temperature oven for the reference performance test (RPT) including a capacity test and an EIS test at different SOCs (see in Table 1). In the capacity test, the battery was charged to 4.2 V with a constant current of 0.5C (1.1 A) and then charged with a constant voltage until the current is less than 0.11 A. Each battery was aged about 1000 equivalent full cycles (EFCs), and a total of 77 charging voltage curves and 355 EIS data (i.e., impedance spectrum) at different SOCs were recorded from the seven batteries.

For model validation, a set of RPT results from calendar aging were used. There are 9 batteries in calendar aging, and the RPT test was performed at different state of health. Finally, 114 groups of EIS and the corresponding charging curve data were obtained. The data also has been divided into two batches, the data with SOC of 30%, 50%, and 70% are used for training, and the data with SOC of 0, 20%, 60%, and 100% are used for prediction. The test condition is shown in Table S1 in support information.

2.2. Coin cell preparation

Fresh positive electrodes (i.e., NMC 532), negative electrodes (i.e., graphite), and lithium-metal (i.e., Li) were used as electrodes to assemble 2032-type coin cells in the following configurations: NMC/Li, graphite/Li, and NMC/graphite, respectively. The diameter of the NMC 532 positive electrode is 14 mm, and the loading is 2.67 mg/cm^2. The graphite negative electrode is 14 mm, and the loading is 1.86 mg/cm^2. The diameter of Li metal is 15.3 mm. The electrolyte was 1 mol $LiPF_6$ dissolved in 1 L solvent with a composition ratio of 1:1 EC and DEC. All coin cells were charged and discharged with a C-rate of 0.05C. The voltage range for NMC/Li, graphite/Li, and NMC/graphite were 2.8–4.2 V, 1.0–0.003 V, and 2.8–4.2 V, respectively.

3. Degradation modes identification from voltage charging curves and EIS

3.1. Degradation identification from charging voltage curves

As battery ages, the increased polarization and materials degradation will result in an upward shift and shortening of the charging voltage plateaus [19]. Differential methods can separate these plateaus and convert them into different peaks in the IC curve and valleys in the DV curve [18]. The IC curve presents the capacity increment ($\frac{dQ}{dV}$) changing with battery voltage (V), where the area between the IC curve and the X-axis corresponds to the capacity contribution in a certain voltage range, as present in Eq. (1). Similarly, DV ($\frac{dV}{dQ}$) curve is obtained by differentiating battery voltage against the capacity, which is used to distinguish the voltage contribution from anode and cathode, and the $\frac{dV}{dQ}$ is shown in Eq. (2) [20].

$$\frac{dQ}{dV} = \frac{\Delta Q}{\Delta V} = \frac{Q_t - Q_{t-1}}{V_t - V_{t-1}} \tag{1}$$

$$\frac{dV}{dQ} = \frac{d(V_{cathode} - V_{anode})}{dQ} = \left(\frac{dV}{dQ}\right)_{cathode} - \left(\frac{dV}{dQ}\right)_{anode} \tag{2}$$

During battery charging, the graphite anode undergoes a lithiation process. In contrast, a delithiation process occurs on the cathode side. Therefore, the voltage increases in the cathode and decreases in the anode resulting in an increased voltage of a full

Table 1
Charge/discharge curves and EIS results from 7 cells.

Batches	Charge/discharge	SOC of EIS tested
Batch #1: Cell 1,3,5,7	0.5C/0.5C	10%, 30%, 50%, 70%, and 90%
Batch #2: Cell 2,6,8		0, 20%, 40%, 60%, 80%, and 100%

battery. To understand the full battery charging process, coin-type half cells and coin-type full cell were assembled; the obtained electrochemical behavior during charging of the three types of coin cells are shown in Fig. 1. In the graphite lithiation process, the voltage decreases step by step corresponding to four consecutive phase transitions from LiC_{24} to LiC_6, which are represented by the discharge plateaus from A1 to A4 (Fig. 1a). The IC curve converts the four lithiation plateaus into peaks at 0.19, 0.13, 0.11, and 0.07 V, corresponding to LiC_{24}, intermediate phase between LiC_{24} and LiC_{18}, LiC_{12}, and LiC_6, respectively (Fig. 1b). Furthermore, the DV curve converts the IC peaks to valleys, which is more convenient for quantifying the capacity contribution of each lithiation plateau (Fig. 1c). For the cathode delithiation process, there are two plateaus named C1 and C2, as shown in Fig. 1(d), which are converted to obvious peaks in the IC curve, corresponding to the oxidation process of Ni^{2+}/ Ni^{3+} and Ni^{3+}/ Ni^{4+}, respectively (Fig. 1e). The capacity increments of cathode are continuously and uniformly distributed over the voltage range, corresponding to the large valleys in the DV curve, and thus the DV peaks caused by the voltage jumps are weak (Fig. 1f).

In the NMC/graphite coin-type full cell charging, there are four charging plateaus, which are caused by both positive oxidation and negative reduction processes (Fig. 1g). The IC curve transforms the charging plateaus into peaks, representing the capacity increment on the voltage scale (Fig. 1h). Among them, peak I is mainly related to the A1 peak of graphite. Peak II and peak IV are too weak to be quantified as they can disappear during battery aging [20]. The highest peak III in the voltage range of 3.65–3.85 V is related to both the phase change of A3 IC peak of the graphite and the C2 IC peak of the NMC. Therefore, the max value of peak III is widely used to study battery aging caused by the loss of active material at the positive and negative electrodes. Dubarry et al.[14,17,21] has used simulation methods to quantify the battery degradation mode of LAM based on Eq. (3), where the subscript low-ercase *1* in the equation indicates the battery in begin-of-life state, and *i* represents the aged cycle number.

In Fig. 1(i), the DV curves of NMC/graphite are similar to the DV curves of graphite, which means that the DV peaks on the full cell are greatly influenced by the phase transition of graphite. Besides, when charging at a low current, the battery capacity for the constant current stage is always regarded as the remaining inventory of lithium [14,21]. Therefore, the endpoint ($\max(Q)_1$) of DV curve is often used to quantify LLI, as described in Eq. (4).

$$LAM_i = \frac{\max\left(\frac{\Delta Q}{\Delta V}\right)_1 - \max\left(\frac{\Delta Q}{\Delta V}\right)_i}{\max\left(\frac{\Delta Q}{\Delta V}\right)_1} \cdot 100 \tag{3}$$

$$LLI_i = \frac{\max(Q)_1 - \max(Q)_i}{\max(Q)_1} \cdot 100 \tag{4}$$

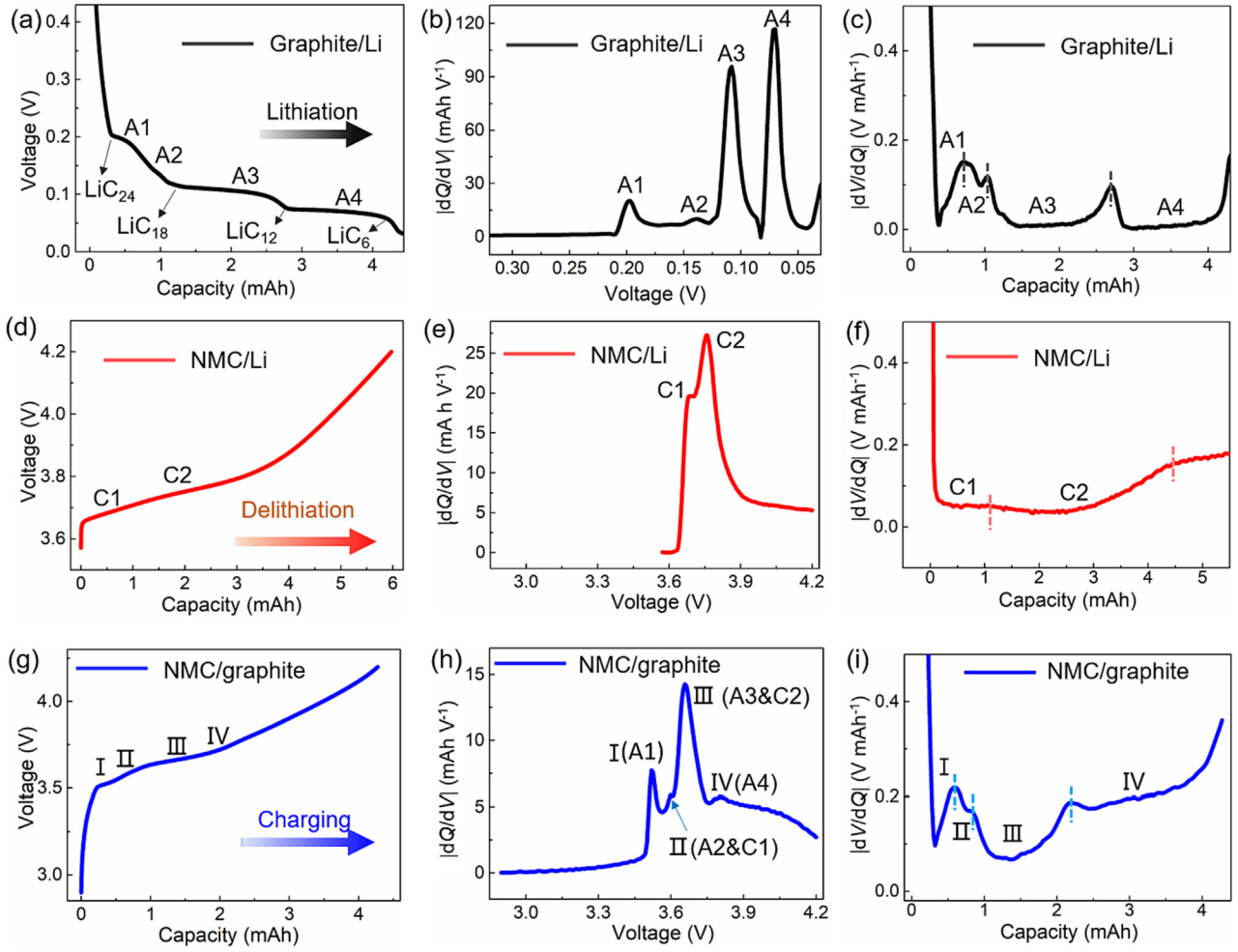

Fig. 1. *Q-V* (left) and IC (middle), and DV (right) curves of graphite/Li (top), NMC/Li (middle), and NMC/graphite (bottom) coin cell to reveal the reaction mechanisms during a full cell charging. The test in graphite lithiation process for (a) Q-V curve and converted to (b) IC and (c) DV curves. The obtained data in NMC delithiation process for (d) Q-V, (e) IC, and (f) DV curves. NMC/graphite data for (g) Q-V, (h) IC, and (i) DV curves.

According to Eqs. (2) and (3), LAM can be quantified by the decrease of the highest peak (III) in the IC curve, which corresponds to the shortening of the main plateau (III) in the charging curve and the decreased depth of the main valley (III) in the DV curve. The endpoint of the DV curve can be used to quantify the LLI, which is the charge capacity contributed by the constant current charging stage in the charge curve. The area between IC curve and X-axis is also can be used to quantify the LLI. The behavior of the charging IC and DV curves and the corresponding relations to the electrodes, as well as the corresponding aging mechanisms, are summarized in Table 2.

3.2. Degradation identification from EIS

EIS test is a powerful technique to analyze battery degradation [22,23]. The EIS results are traditionally presented in a Nyquist plot presenting the battery impedance spectrum, as shown in Fig. 2. As the test frequency decreases from 6500 Hz to 0.01 Hz, the EIS spectrum shows two intersecting semicircles followed by a straight line, which can be fitted by an Equivalent Circuit Model. Then, an electrochemical meaning is given, where the first semicircle diameter represents the solid electrolyte interphase resistance (R_{sei}) and the second semicircle diameter represents the charge transfer resistance (R_{ct}), while the slope of the line is related to the diffusion of lithium ions [18].

The battery degradation modes are widely analyzed by EIS. After cycling, the SEI film forms on the anode surface, which is a limit link for Li-ions diffusion between the electrolyte and the anode [24]. Besides, the SEI film is mainly composed of lithium compounds generated from side reactions e.g., decomposition of electrolyte and metal deposition, resulting in an irreversible loss of lithium inventory. Furthermore, some lithium plating occurs on the anode surface that can react with electrolyte, resulting in lithium compounds, hindering the charge transfer [25]. Hence, LLI is related to the R_{sei} and R_{ct}.

As reported in [15], the LAM is related to the diffusion coefficient (D_{Li+}), because the diffusion of lithium ions within the electrolyte and active electrode materials is controlled by the particle size and the available surface area of the electrode material. The D_{Li+} can be calculated by Eq. (5), where R represents the gas constant, T is the absolute temperature, A is the electrode surface, n is the number of electrons transferred per molecule, F is the Faraday's constant, C is the Li-ions concentration, and the variable Y_0 is a function of Warburg impedance coefficient (σ) in Eq. (6). The σ is related to the slope of the tail of the EIS spectrum, and calculated by Eq. (7), where ω is the angular frequency used in the EIS measurements. Therefore, it can be concluded that the LAM is related to Y_0.

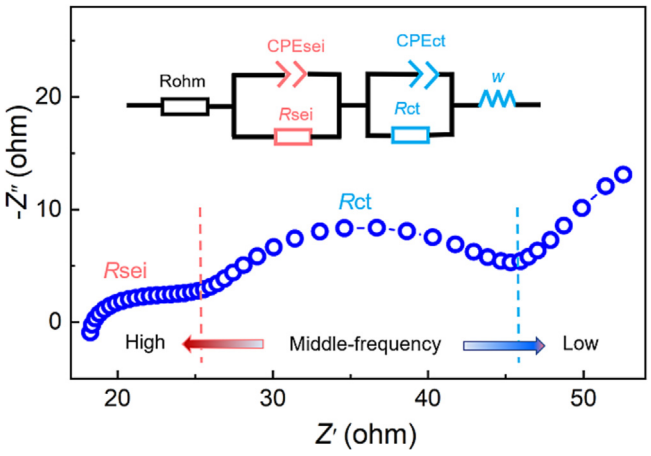

Fig. 2. Composition of a normal electrochemical impedance spectrum.

$$D_{Li^+} = \frac{R^2T^2{Y_0}^2}{A^2C^2n^4F^4} \quad (5)$$

$$Y_0 = \frac{1}{\sigma\sqrt{2}} \quad (6)$$

$$Z_{re} = R_{ohm} + R_{ct} + \sigma\omega^{-1/2} \quad (7)$$

Hence, LLI is related to R_{sei} and R_{ct}, which correspond to the two semicircles in the high-frequency and mid-frequency regions of the impedance spectrum. Furthermore, the LAM is related to the Y_0 that corresponds to the tail in the low-frequency region of the impedance spectrum. Based on these relationships, the EIS was widely used to quantify the degradation contribution from each aging mode by Eq. (8) and Eq. (9) [14,15].

$$LLI = 100\frac{(R_{sei,i} + R_{ct,i}) - (R_{sei,1} + R_{ct,1})}{R_{sei,1} + R_{ct,1}} \quad (8)$$

$$LAM = 100\frac{(Y_{0,1} - Y_{0,i})}{Y_{0,1}} \quad (9)$$

Table 3
Relationship between the impedance spectrum and the most pertinent degradation modes.

AR-ECM component	Most pertinent DMs
Increase in R_{sei} and R_{ct}	LLI Quantified by Eq. (8)
Increase in Y_0	LAM Quantified by Eq. (9)

Table 2
Relationship between the behaviors of charge, IC, and DV curves and the most pertinent degradation modes for graphite/Li, NMC/Li and NMC/graphite.

Change in charge curve	Change in IC curve	Change in DV curve	Most pertinent DMs
Full cell: smaller charging capacity, and upward trend. Anode: smaller lithiation capacity, and upward trend. Cathode: smaller delithiation capacity, and upward trend.	Full cell: shift toward lower or higher voltage, decrease of the height of the peaks. Anode: shift toward higher or lower voltage. Cathode: shift toward lower or higher voltage.	Full cell: shift toward lower capacity. Anode: shift toward lower capacity. Cathode: shift toward lower capacity.	LLI Quantified by Eq. (4)
Full cell: shorten of main plateau (III) Anode: shorten of A3 plateau. Cathode: shorten of C2 plateau.	Full cell: decrease of the highest peak (III). Anode: decrease of the A3 peak Cathode: decrease of the C2 peak	Full cell: decrease the depth of the main valley (III). Anode: decrease of the depth of the A3 valley. Cathode: decrease of the depth of the A3 valley.	LAM Quantified by Eq. (3)

Similarly, the subscript *1* in the Eq. (8) and (9) indicates the battery in begin-of-life state, and *i* represents the aged cycle number. With these equations, the relationship between the parameters change of the impedance spectrum and the aging modes can be summarized in Table 3.

3.3. Degradation in a full cell case

Periodic RPTs during battery aging were performed to quantify the incremental degradation of the cells, as explained in Section 2; the evaluation of the charging curve, measured at 0.5C (i.e., 1.1 A),

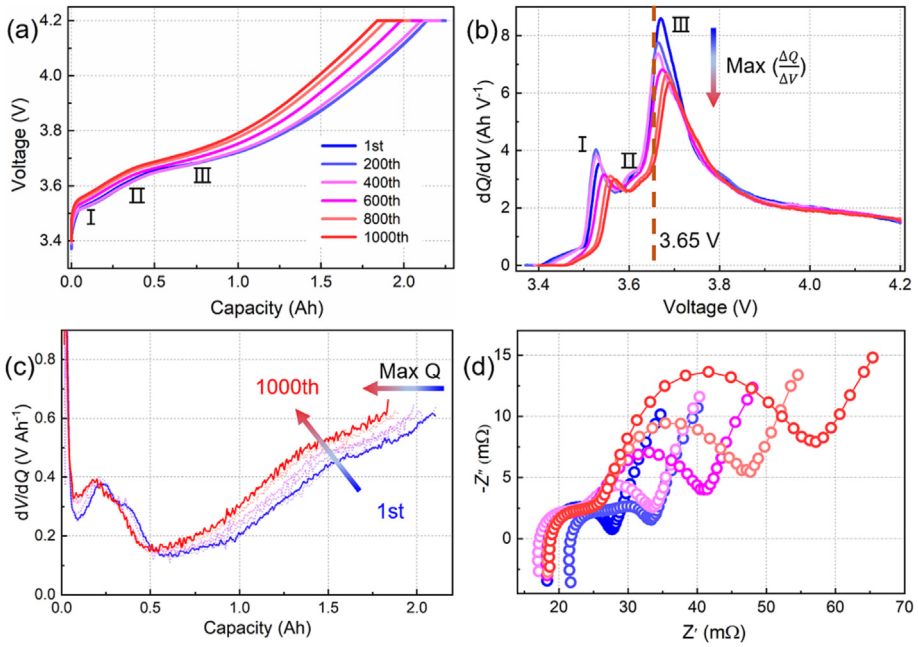

Fig. 3. Periodic reference performance tests (RPTs) for one of the aged batteries before aging and at the 200th, 400th, 600th, 800th, and 1000th cycles, including (a) constant current-constant voltage charges curves, (b) IC curve obtained by differentiating the charging curve, (c) DV curves, and (d) corresponding EIS results obtained at 50% SOC.

Table 4
The relationship between changes in charge curve and changes in impedance spectrums and the details of degradation mechanisms.

Changes in the voltage charging curve	Changes in the impedance spectrum	Most pertinent DM	Potential aging mechanisms
Decrease in charging capacity, and left and upward shifting.	Increase in R_{sei} and R_{ct}	LLI Quantified by Eqs. (4) & (8)	Electrolyte decomposition; oxidation of electrolyte; Lithium plating; formation of Li grains; solvent co/intercalation.
Shorten of main plateau (3.65–3.75 V)	Increase in Y_0	LAM Quantified by Eqs. (3) & (9)	Electrode decomposition; oxidation of the electrolyte; intercalation gradient strains in the active particles; formation of Li grains; crystal structure disordering; transition metal dissolution.

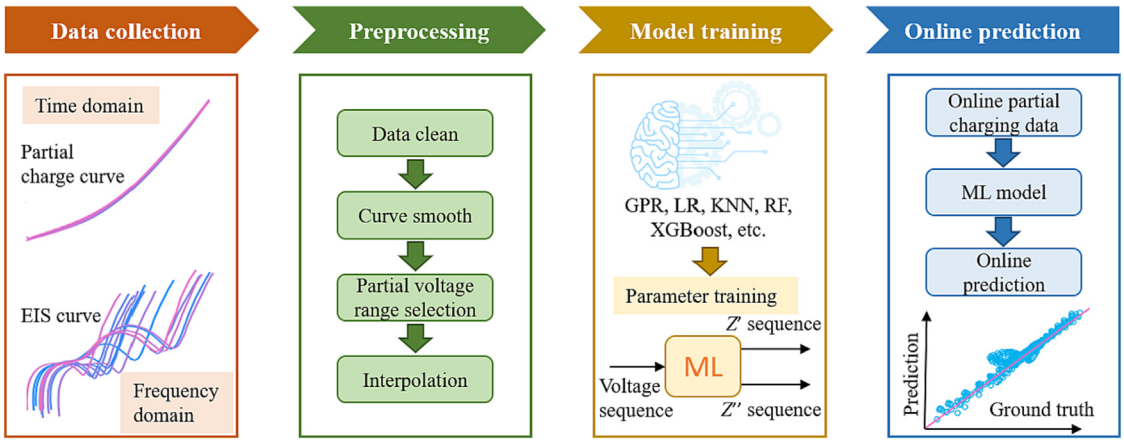

Fig. 4. Overall framework for the machine learning-based EIS prediction with partial charging curves.

and the evaluation of the impedance spectrum, recorded at 50% SOC, are presented in Fig. 3. As shown in Fig. 3(a), with the battery aging, the charging voltage plateaus show an upward trend and move to the left, corresponding to an increased internal impedance and a reduction of battery capacity, respectively. For the first 400 cycles, three distinct voltage plateaus I, II and, III could be identified. As the battery ages, all three plateaus become shorter, and the most subtle phase II plateau becomes indistinguishable. Converting the voltage-capacity curve to the IC peak in the voltage range (Fig. 3b), the obtained peaks decrease and shift to the right, behavior which is associated with increased internal resistance and loss of active material. As analyzed in section 3.1, peak I is mainly controlled by the graphite reduction potential. Peak II is almost indistinguishable, and it disappears after a few hundred cycles. The main peak III (3.65—3.75 V) is controlled by both the reduction potential of the graphite anode and the oxidation potential of the NMC cathode, so the decreasing trend of peak III in height (max $\frac{\Delta Q}{\Delta V}$) can reflect the degree of loss of positive and negative active materials. In addition, the loss of lithium ions is usually manifested as a leftward shift of the DV curve, as shown in Fig. 3(c). The max Q decrease with the battery aging, and at the same time, the DV curves shift upwards and left. This is consistent with the aging results speculated in Section 3.1.

The corresponding battery EIS results are shown in Fig. 3(d). With the battery aging, R_{sei} and R_{ct} show an increasing trend, from less than 10 to over 50 mΩ. As discussed in Section 3.2, the

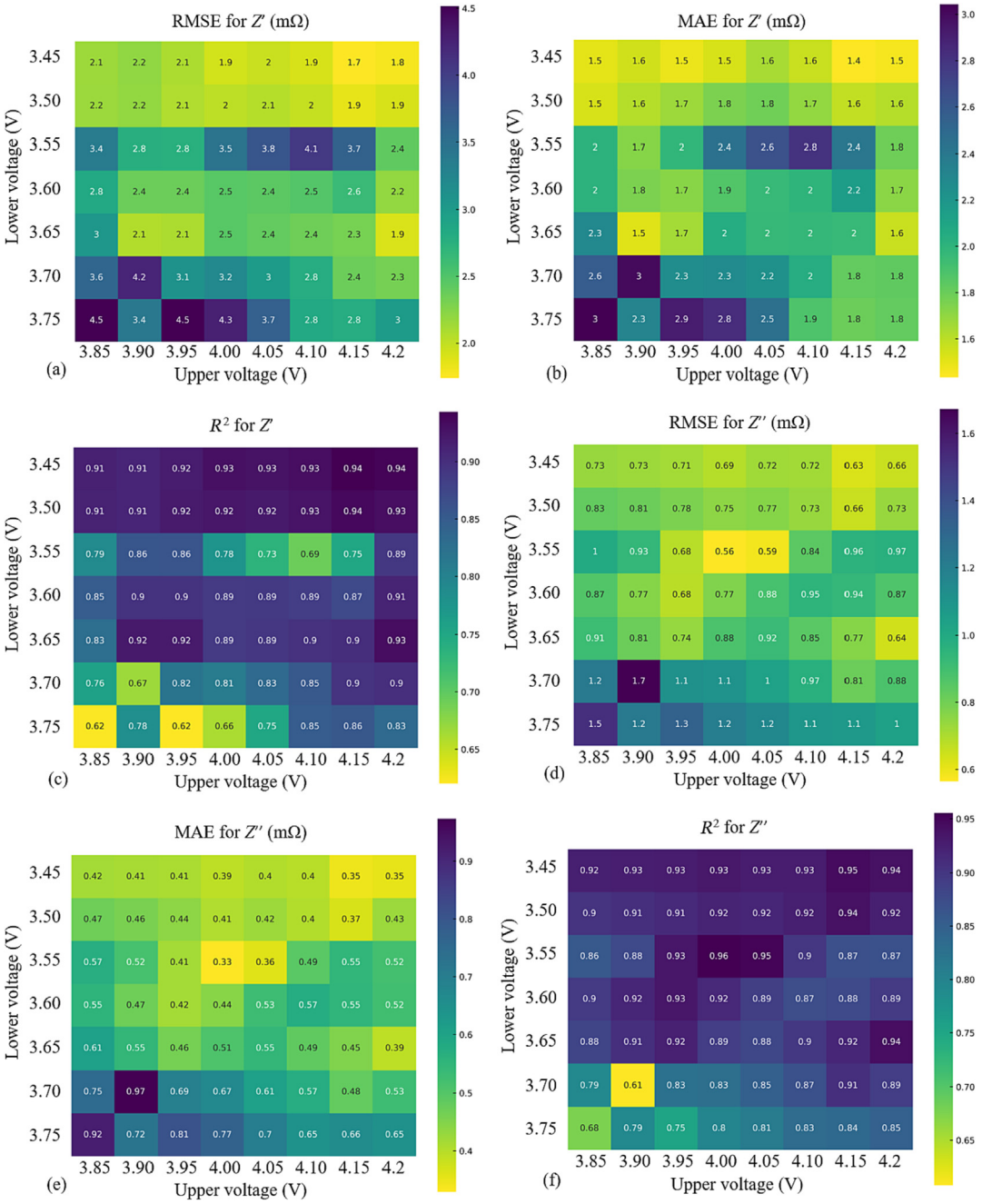

Fig. 5. The EIS curve prediction evaluations with different input voltage range for 50% SOC. (a) The RMSE for the Z'; (b) the MAE for the Z'; (c) the R^2 between the predicted Z' and the ground truth; (d) the RMSE for the Z''; (e) the MAE for the Z''; (f) the R^2 between the predicted Z'' and the ground truth.

increased R_{sei} in the high-frequency region and R_{ct} in the middle frequency region represents an increase in LLI. Besides, the tail of the impedance spectrum associated with the Li-ion diffusion shows a decrease in slope with the battery aging, corresponding to a decreased Y_0. The above aging trends and the corresponding degradation modes and aging mechanisms are summarized in detail in Table 4. Since the IC and DV curves contain inherent information to the charging voltage curves, Table 4 only summarizes the changes observed in the charging curve.

Based on the quantifiable relationships between Eq. (4) and Eq. (8) and between Eq. (3) and Eq. (9), it is possible to establish an accurate physical functional relationship between the charging curve and impedance spectrum parameters. In other words, the impedance parameters can be obtained based on the parameters of the charging voltage curve and vice-vaersa. However, this is not practical; on the one hand, the algorithm needs to adjust the algorithm parameters according to different batteries, different working conditions or even different environments. On the other hand, the extraction of input features can be uncertain due to the charging voltage curves containing lots of feature parameters. Most of these issues can be overcome by using machine learning, which allows for algorithm self-selection, adaptability, fast speed, and high accuracy advantages [26] and can be performed to predict the EIS.

In this work, the max $\frac{\Delta Q}{\Delta V}$ appears in the voltage internal 3.65–3.75 V in the IC curve, and will be used to estimate the impedance spectrum at low frequency, since both the max $\frac{\Delta Q}{\Delta V}$ and the low-frequency impedance spectrum can be used to quantify the same degradation mode, i.e., LAM. Transforming the charging curve into an IC curve requires a smoothing process, which can cause data distortion (especially of the charging plateau). Therefore, we recommend using the charging curve directly to predict the EIS rather than converting it to the IC curve. Besides, the lithium loss estimates associated with R_{sei} and R_{ct} usually require the battery capacity at the cut-off voltage. However, in real-life application, it is almost impossible to fully discharge a battery before recharging it, making it difficult to obtain a complete voltage capacity curve as well as a normal capacity. The trend of "left and upward shifting" used to indicate the lithium loss may be obtained from the partial charge curve. Therefore, partial/complete charging curves will be used to predict the complete EIS by machine learning methods.

4. Impedance spectrum prediction

4.1. Prediction framework

The proposed framework for the EIS prediction with partial charging curves is shown in Fig. 4. Firstly, the charging voltage curve and the EIS curve at different SOCs are collected. Then the data are preprocessed, where the data are cleaned first. The abnormal values are filtered, and the missing values are filled up in this process. In addition, the curve is filtered to remove the noise. The partial voltage range is selected according to the practical requirements and the electrochemical analysis in the above section and the charging voltage curve is interpolated in this range based on the voltage interval selected as 5 mV in this paper. The third step is to train the machine learning model via the processed data. Different machine learning models could be selected including gaussian process regression (GPR) [27], linear regression (LR) [28], K-nearest neighbors (KNN) regression [29], XGBoost [30], artificial neural network (ANN) [31], and random forest (RF) [32], which helps evaluate the generalization and robustness of the prediction framework with various machine learning models. The details model algorithms of each machine learning method can be obtained from the corresponding literature. The prediction framework is a sequence-to-sequence way, where the voltage sequence is the input while the outputs are the predicted Z' and Z'' sequences. The parameters of the machine learning models are trained using the training data. Finally, the trained model is used for the online prediction with the obtained online measured partial voltage data. The predictions of the EIS curves at different SOCs could be obtained by this prediction framework. The prediction results based on the proposed framework are presented and evaluated in the following sections.

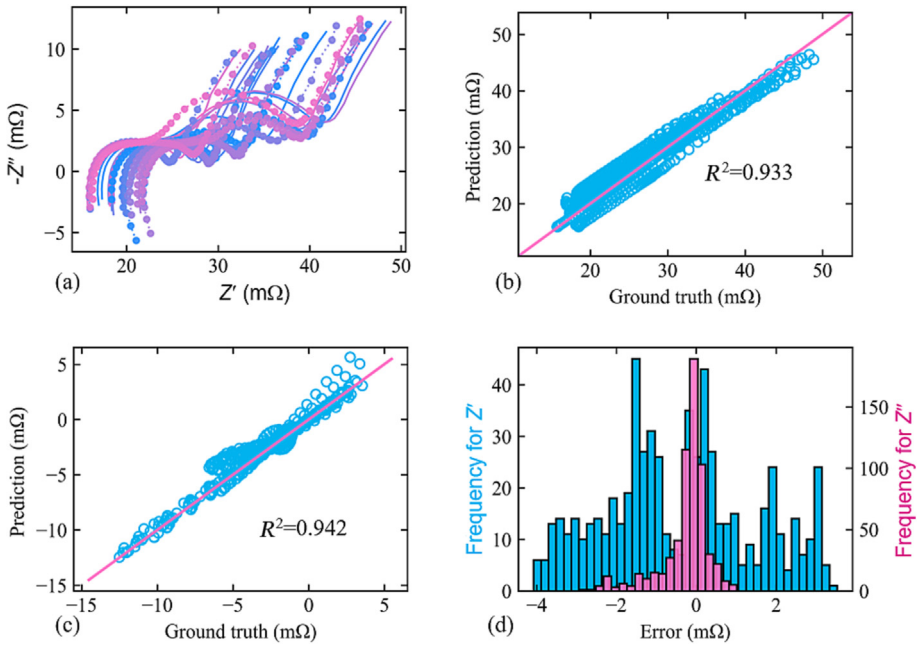

Fig. 6. The EIS curve prediction results with the input voltage range from 3.65 to 4.2 V for 50% SOC. (a) The predicted curve (dotted lines) and the real curve (solid lines). (b) The mapping between the predicted Z' and the real Z'. (c) The mapping between the predicted Z'' and the real Z''. (d) Frequencies of the errors for the predicted Z' and Z''.

4.2. Prediction with the different voltage range

Firstly, the different partial charging voltage curves (according to the available voltage range in practical applications) are used as input to predict the whole EIS curve. The GPR model is used as the machine learning model for the evaluations [33]. The predictions of the EIS curves at 50% SOC are demonstrated. Here, the batteries with EIS tests at odd SOC points are used, where 41 samples are included. 70% of them (i.e., 28 samples) are used for training and 30% (i.e., 13 samples) are used for validations.

The root means square error (RMSE), mean absolute error (MAE), and the fitted *R* square (R^2) between the predicted values and the ground truth with different voltage ranges are shown in Fig. 5, where both the errors and R^2 for the *Z*' and *Z*'' are included. It is wished that the less the RMSE and MAE, the better, and the higher the R^2, the better. The results show that generally the errors become larger and R^2 becomes smaller with the decrease of voltage range, which means generally wider voltage range contains more information that supports better predictions. However, the results show that the voltage range from 3.65 to 4.2 V also provides satisfactory predictions. These confirm the above mechanism analysis suggesting that the main charging plateau (3.65–3.75 V) derived from the partial charging curve that can represent shift characteristics of the whole curve, which can accurately predict the impedance spectrum. As a result, the voltage ranges that have satisfactory prediction accuracy all contain 3.65–3.75 V.

Therefore, the aging mechanism analysis and the correlation evaluation among the charging curve, IC / DV curve, and the EIS curve help select the proper partial voltage range that can offer physical interpretations and has high performance. This voltage range (i.e., 3.65–4.2 V) is used in the following evaluations for other aspects.

The prediction results for the EIS curve at 50% SOC using the voltage range from 3.65 to 4.2 V are shown in Fig. 6, where the predicted curve (dotted lines) and the real curve (solid lines) are shown in Fig. 6(a), the mapping between the predicted *Z*' and the ground truth is shown in Fig. 6(b), the mapping between the predicted *Z*'' and the ground truth is shown in Fig. 6(c), and the error occurances of the *Z*' and *Z*'' are shown in Fig. 6(d). The results show that the predicted curves fit well with the real curves, where both the fitting of the predicted *Z*' and the *Z*'' show highly linear mappings with the real values with R^2 of 0.933 and 0.942, respectively. The histogram of occurances of the errors of the predicted *Z*' and *Z*'' illustrate that the errors are within 4 mΩ for *Z*' and most of the errors are less than 2 mΩ for *Z*''. Therefore, the results proved that the predicted curves are close to the real curves for all the tests.

4.3. Prediction at different SOCs

Then, the model is evaluated based on the predictions of the EIS curves at different SOC points to prove the generalization of the proposed method at different SOC levels. The machine learning model and the test ratio are set similarly as in the previous section, i.e., GPR model and 30% testing ratio. The RMSE, MAE, and R^2 for the predicted *Z*' and *Z*'' are shown in Fig. 7, while the numerical results are listed in Table 5 and Table 6, respectively for batch#1 and batch#2. The accurate prediction results prove that the prediction model is suitable for being applied over a wide SOC range, which means the EIS curve at different SOC points under different aging status could be predicted. Therefore, the generalization of the prediction model is accurate, which supports different application requirements. The obtained results show that all the RMSE and MAE are less than 2.8 mΩ and 1.2 mΩ for the *Z*', all the RMSE and MAE are less than 1.7 mΩ and 1.1 mΩ for the *Z*''. The R^2 for the *Z*' and *Z*'' are larger than 0.875 and 0.915 respectively, which means that the predicted values are converged to the real values at all the SOC stages. The results indicate that the prediction errors for the 20%–80% SOC are less than those in 0–10% and 90–100% SOC stages. This may be related to the electrochemical stability of the battery at a moderate SOC range [34].

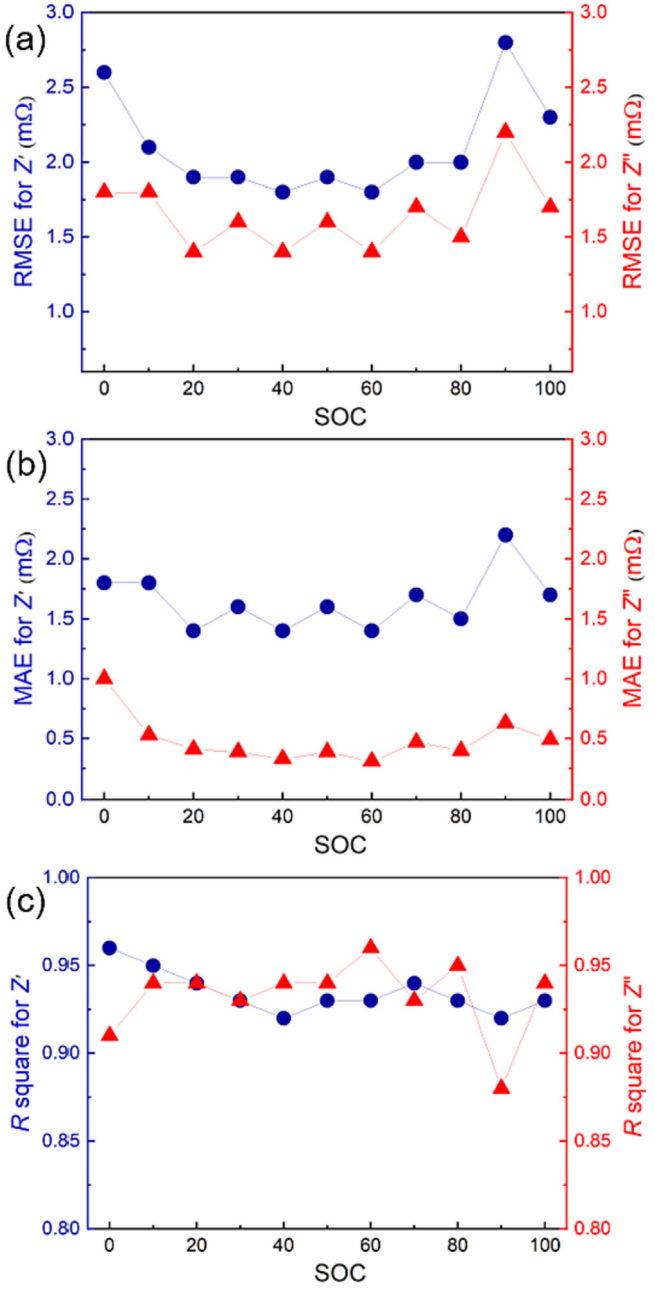

Fig. 7. Prediction evaluation for different SOCs. (a) results for RMSE, (b) results for MAE, (c) results for R^2.

4.4. Robustness evaluation

Finally, the robustness of the proposed prediction method is evaluated for different training – testing ratios and considering different ML algorithms. The errors and the fitted R^2 of the prediction results are shown in Fig. 8. Generally, with the reduction of the training data, the errors become larger and the R^2 becomes smaller, which means the performance becomes poorer with the reduction of data for the model training. However, the results show that even

Table 5
Results for different SOC with 30% data for testing for batch #1.

Index	10% SOC	30% SOC	50% SOC	70% SOC	90% SOC
RMSE of Z' (mΩ)	2.103	1.909	1.902	2.044	2.784
MAE of Z' (mΩ)	1.789	1.569	1.574	1.670	2.175
R^2 of Z'	0.953	0.932	0.933	0.941	0.921
RMSE of Z'' (mΩ)	0.846	0.625	0.644	0.807	1.173
MAE of Z'' (mΩ)	0.533	0.391	0.392	0.466	0.632
R^2 of Z'' (mΩ)	0.936	0.930	0.942	0.928	0.875

Table 6
Results for different SOC with 30% data for testing for batch #2.

Index	0% SOC	20% SOC	40% SOC	60% SOC	80% SOC	100% SOC
RMSE of Z' (mΩ)	2.648	1.874	1.808	1.826	2.014	2.298
MAE of Z' (mΩ)	1.822	1.403	1.396	1.438	1.534	1.683
R^2 of Z'	0.959	0.938	0.916	0.929	0.933	0.931
RMSE of Z'' (mΩ)	1.698	0.632	0.543	0.545	0.651	0.790
MAE of Z'' (mΩ)	1.032	0.407	0.325	0.313	0.399	0.493
R^2 of Z'' (mΩ)	0.913	0.938	0.945	0.964	0.951	0.943

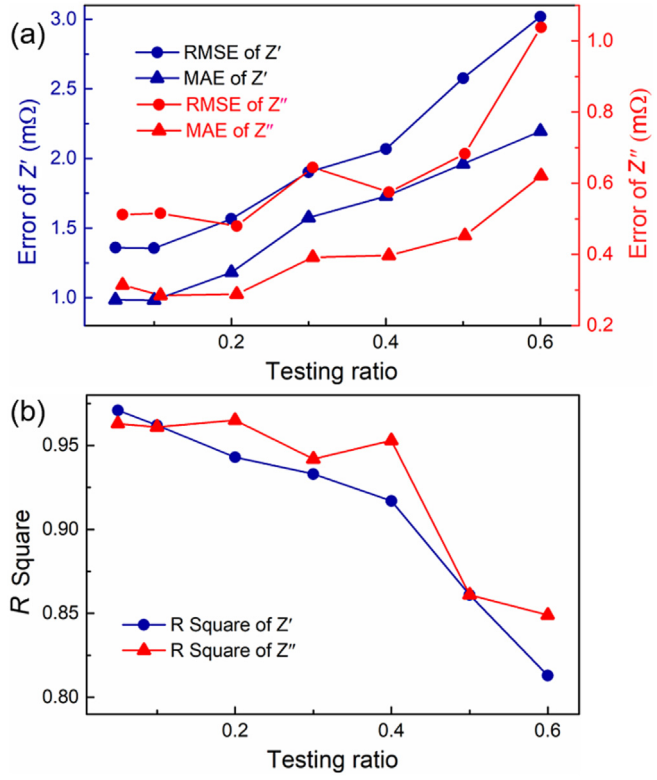

Fig. 8. Errors and the fitted R^2 with different ratios of data for validation.

with 40% data for training (16 samples) and 60% data for validation (25 samples), the RMSE and MAE for Z' are still within 3.02 mΩ and 2.2 mΩ respectively, those for Z'' are still less than 1.04 mΩ and 0.63 mΩ, respectively (Fig. 8a). The R^2 for Z' and Z'' are still 0.813 and 0.849 respectively (Fig. 8b). Therefore, the model has good robustness with the reduction of training data and can still with satisfactory predict performances.

In order to evaluate the robustness of the proposed prediction framework, different machine learning algorithms are used. The detailed process of each machine learning algorithm is described in supporting note 1. The prediction results are listed in Table 7, while the errors of each machine learning model are shown in Fig. S1. The results are obtained by the prediction for the EIS curve at 50% SOC using 30% data for validation. One can conclude that different machine learning algorithms are suitable for the prediction of the EIS curve with the proposed framework. Among them, the GPR has the best accuracy performance, and the calculation time is also proper for online applications with only 0.598 s in total for the whole training and prediction process.

Finally, we test our model on the prediction for calendar aging batteries. The same set of the results for Fig. 6 is used. The prediction results are shown in Fig. 9, which indicates that our model is also suitable for the prediction under calendar aging. The fitted R^2 between the predictions and the ground truth is larger than 0.944. The errors are less than 1.5 mΩ for Z'' and 4 mΩ for Z'. The RMSEs for Z' and Z'' are 1.38 and 0.36 mΩ, respectively, while the MAEs are 0.93 and 0.23 mΩ, respectively. Therefore, our method is robust for the EIS prediction under both cycling aging and calendar aging using a partial charging curve.

Table 7
Comparisons with different machine learning algorithms.

Index	GPR	LR	RF	XGBoost	KNN	ANN
RMSE of Z' (mΩ)	1.902	5.337	2.341	3.234	2.133	3.353
MAE of Z' (mΩ)	1.574	2.921	1.790	2.120	1.475	2.352
R^2 of Z'	0.933	0.470	0.898	0.805	0.915	0.791
RMSE of Z'' (mΩ)	0.644	1.481	0.860	1.055	0.730	1.122
MAE of Z'' (mΩ)	0.392	0.829	0.477	0.640	0.427	0.708
R^2 of Z'' (mΩ)	0.942	0.692	0.896	0.844	0.925	0.823
Time (s)	0.598	0.002	1.362	1.539	0.002	4.589

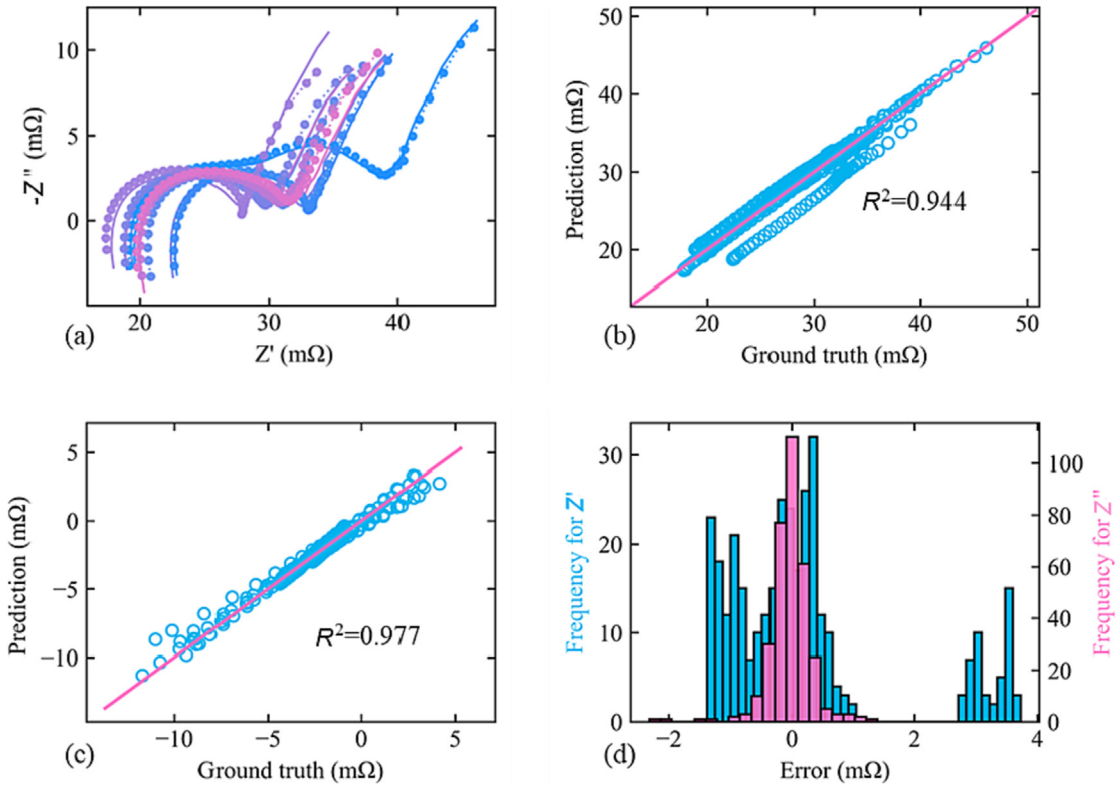

Fig. 9. The EIS curve prediction results under calendar aging. (a) The predicted curve (dotted lines) and the real curve (solid lines). (b) The mapping between the predicted Z' and the real Z'. (c) The mapping between the predicted Z'' and the real Z''. (d) Frequencies of the errors for the predicted Z' and Z''.

5. Conclusions

In this study, an accurate impedance spectrum prediction from charging voltage curves is achieved by machine learning methods, based on the mechanism that both charging curves and impedance spectrum can achieve the quantification of LAM and LLI. Coin cells were assembled to clarify the electrochemistry mechanisms of IC and DV curves at the electrodes level. The results support that the main peak in the IC curve (3.65–3.75 V) can be used to quantify the LAM, and the shifting trend of DV curve can be used to quantify LLI. Furthermore, the high and medium frequency impedance spectrum that represents R_{sei} and R_{ct} can be used to quantify the LLI, and the low frequency impedance spectrum indicating the diffusion of Li-ions can be used to quantify the LAM. Therefore, a quantifiable potential mechanistic relationship supports the prediction of EIS by charging curves.

Consistent with the mechanistic analysis, machine learning can achieve accurate EIS predictions. We optimized the voltage input interval for prediction and found that it is necessary to include the range 3.65–3.75 V in the input voltage in order to obtain an accurate result, which is consistent with the internal mechanism analysis between the IC curve and EIS. When the input voltage range is 3.65–4.2 V, reliable results are obtained most of the time with RMSEs less than 1.9 mΩ. The majority of the predictions are less than 4 mΩ with independent of the considered charging voltage ranges. Besides, the impedance spectrum predictions for battery at different SOCs was also realized. Furthermore, we varied the proportion of the data set for training and applied different machine learning methods to evaluate the robustness and generalization of the proposed method. We can conclude that 40% data is enough to obtain an impedance spectrum prediction result with RMSEs less than 3 mΩ. Among the considered ML algorithms, the GPR with multiple outputs model is recommended as the proper choice because of the high accuracy and acceptable computational burden.

Declaration of competing interest

The authors declare that they have no known competing financial interests or personal relationships that could have appeared to influence the work reported in this paper.

Acknowledgments

Jia Guo is supported by a grant from the China Scholarship Council (202006370035), and a fund from Otto Monsteds Fund (4057941073). We would also like to thank Haidi Energy Technology Co. for providing electrodes, which were used to manufacture the coin cells.

Appendix A. Supplementary material

Supplementary data to this article can be found online at https://doi.org/10.1016/j.jechem.2023.01.004.

References

[1] Y. Che, Y. Zheng, Y. Wu, X. Sui, P. Bharadwaj, D. Stroe, Y. Yang, X. Hu, R. Teodorescu, Appl. Energy 323 (2022).
[2] X.Z. Fan, M. Liu, R. Zhang, Y. Zhang, S. Wang, H. Nan, Y. Han, L. Kong, Chin Chem. Lett. 33 (2022) 4421–4427.
[3] X. Liu, H.J. Peng, B.Q. Li, X. Chen, Z. Li, J.Q. Huang, Q. Zhang, Angew Chem. Int. Ed 134 (48) (2022) e202214037.
[4] X. Liu, X.Q. Zhang, X. Chen, G.L. Zhu, C. Yan, J.Q. Huang, H.J. Peng, J. Energy Chem. 68 (2022) 548–555.
[5] L. Wu, K. Liu, H. Pang, Electrochim. Acta 368 (2021).
[6] Y. Che, D. Stroe, X. Hu, R. Teodorescu, IEEE Trans Industr Inform (2022) 1–10.

[7] M.A. Zabara, G. Katlrcl, B. Ülgüt, J. Phys. Chem. C 126 (2022) 10968–10976.
[8] J. Meng, M. Ricco, G. Luo, M. Swierczynski, D.I. Stroe, A.I. Stroe, R. Teodorescu, IEEE Trans. Ind. Appl. 54 (2018) 1583–1591.
[9] X. Hu, H. Yuan, C. Zou, Z. Li, L. Zhang, IEEE Trans. Veh. Technol. 67 (2018) 10319–10329.
[10] K. Mc Carthy, H. Gullapalli, K.M. Ryan, T. Kennedy, J. Electrochem. Soc. 168 (2021).
[11] Y. Zhang, Q. Tang, Y. Zhang, J. Wang, U. Stimming, A.A. Lee, Nat. Commun. 11 (2020) 6–11.
[12] P. Jones, U. Stimming, A.A. Lee, Nat. Commun. 13 (2022) 4806.
[13] Y. Duan, J. Tian, J. Lu, C. Wang, W. Shen, R. Xiong, Energy Storage Mater 41 (2021) 24–31.
[14] C. Pastor-Fernández, K. Uddin, G.H. Chouchelamane, W.D. Widanage, J. Marco, J. Power Sources 360 (2017) 301–318.
[15] E. Teliz, C.F. Zinola, V. Díaz, Electrochim. Acta 426 (2022).
[16] J. Guo, S. Jin, X. Sui, X. Huang, Y. Xu, Y. Li, D.W. Peter, K. Kristensen, D.-I. Stroe, J. Mater. Chem. 11 (2022) 41–52.
[17] M. Dubarry, C. Truchot, B.Y. Liaw, J. Power Sources 219 (2012) 204–216.
[18] J. Guo, Y. Li, J. Meng, K. Pedersen, L. Gurevich, D. Stroe, J. Energy Chem 74 (2022) 34–44.
[19] M. Ouyang, Z. Chu, L. Lu, J. Li, X. Han, X. Feng, G. Liu, J. Power Sources 286 (2015) 309–320.
[20] R. Xiong, Y. Pan, W. Shen, H. Li, F. Sun, Renewable Sustain. Energy Rev. 131 (2020).
[21] G. Seo, J. Ha, M. Kim, J. Park, J. Lee, E. Park, S. Bong, K. Lee, S.J. Kwon, S. Pil Moon, J. Choi, J. Lee, J. Energy Chem. 67 (2022) 663–671.
[22] Y. Chen, Y. Li, W. Li, G. Cao, S. Tang, Q. Su, S. Deng, J. Guo, Electrochimica Acta 281 (2018) 48–59.
[23] J. Guo, W. Li, ACS Appl. Energy Mater. 5 (2022) 397–406.
[24] J. Zhu, M. Knapp, D.R. Sørensen, M. Heere, M.S.D. Darma, M. Müller, L. Mereacre, H. Dai, A. Senyshyn, X. Wei, H. Ehrenberg, J. Power Sources 489 (2021).
[25] X. Lin, K. Khosravinia, X. Hu, J. Li, W. Lu, Prog. Energy Combust. Sci 87 (2021).
[26] X. Chen, X. Liu, X. Shen, Q. Zhang, Angew. Chem. Int. Ed 60 (2021) 24354–24366.
[27] X. Hu, Y. Zheng, X. Lin, Y. Xie, IEEE Trans. Transp. Electrification 6 (2020) 427–438.
[28] X. Sui, S. He, S.B. Vilsen, J. Meng, R. Teodorescu, D.I. Stroe, Appl. Energy 300 (2021).
[29] Z. Wei, Q. He, Y. Zhao, J. Power Sources 549 (2022).
[30] S. Song, C. Fei, H. Xia, Energies 13 (2020) 812.
[31] V. Chandran, C.K. Patil, A. Karthick, D. Ganeshaperumal, R. Rahim, A. Ghosh, World Electr. Veh. J 12 (2021) 38.
[32] K.S.R. Mawonou, A. Eddahech, D. Dumur, D. Beauvois, E. Godoy, J. Power Sources 484 (2021).
[33] X. Hu, Y. Che, X. Lin, S. Onori, IEEE Trans. Transp. Electrification 7 (2021) 382–398.
[34] J. Jiang, W. Shi, J. Zheng, P. Zuo, J. Xiao, X. Chen, W. Xu, J.-G. Zhang, J. Electrochem. Soc. 161 (2014) A336–A341.